JOURNAL OF PROPULSION AND POWER
Vol. 24, No. 3, May–June 2008

Numerical and Experimental Investigations of Crossover Ion Impingement for Subscale Ion Optics

Joseph Wang,* Yong Cao,† and Raed Kafafy†
Virginia Polytechnic Institute and State University, Blacksburg, Virginia 24061-0203
and
Rafael Martinez‡ and John Williams§
Colorado State University, Fort Collins, Colorado 80523

DOI: 10.2514/1.33793

A coordinated experimental and modeling study is carried out to investigate the crossover ion impingement of the accelerator grid for a seven-aperture gridlet. Simulations from a new three-dimensional global gridlet model reveal the differences in beamlet profile and accelerator-grid impingement pattern between the center aperture and an edge aperture on the accelerator grid at near-crossover operating conditions. It is shown that simulation predictions of the accelerator-grid impingement-current characteristics and the crossover limits agree well with those from measurements.

Nomenclature

d	=	hole diameter
$\mathbf{E}$	=	electric field vector
e	=	electron charge, 1.602×10^{-19} C
$\mathbf{F}$	=	force vector
J	=	current
l	=	spacing, thickness
n	=	number density
T	=	temperature
t	=	grid thickness
V	=	voltage
$\mathbf{v}$	=	velocity vector
$\mathbf{x}$	=	position vector
λ_D	=	Debye length
Φ	=	electrostatic potential

Subscripts

a	=	acceleration grid
b	=	beamlet
cc	=	center to center
cex	=	charge exchange
e	=	electron
exp	=	experimental result
g	=	gap between ion optics grids
imp	=	direct ion impingement
leak	=	leakage current
N	=	net acceleration
num	=	numerical result
s	=	screen grid
T	=	total acceleration
0	=	upstream plasma condition
∞	=	downstream plasma condition

Presented as Paper 5244 at the 43rd AIAA/ASME/SAE/ASEE Joint Propulsion Conference, Cincinnati, 9–11 July 2007; received 31 July 2007; accepted for publication 25 February 2008.

*Associate Professor, Department of Aerospace and Ocean Engineering; jowang@vt.edu. Associate Fellow AIAA.
†Postdoctoral Fellow, Department of Aerospace and Ocean Engineering.
‡Graduate Research Assistant, Department of Mechanical Engineering.
§Assistant Professor, Department of Mechanical Engineering.

I. Introduction

THE behavior of the accelerator-grid current defines the operational envelope of an ion optics system. Under normal operating conditions, the ions in the discharge plasma upstream of the screen grid should form focused ion beamlets when extracted and accelerated through the optics. However, if the discharge plasma density is too low for given grid voltages, the ion beamlet may become overfocused by the shape of the upstream sheath, resulting in crossover ion impingement on the acceleration grid. The onset of direct impingement by overfocused beam ions is referred to as the *crossover limit*. On the other hand, if the discharge plasma density is too high, the ion beamlet may become underfocused, resulting in direct interception of beam ions by the acceleration grid. The onset of direct impingement by underfocused beam ions is referred to as the *perveance limit*. Thruster operation that results in direct impingement can cause excessive sputter erosion of the accelerator grid, which is one of the direct causes for ion-thruster failure. Hence, an accurate prediction of the crossover limit, the perveance limit, and ion impingement under these conditions is extremely important for ion optics design.

Many computer particle simulation models have been developed in recent years to study plasma flow in ion optics (see, for example, [1–16] and references therein). Most ion optics models are either axisymmetric models or three-dimensional models constructed for a cross section of one-twelfth of a single aperture using the sixfold hexagonal symmetry of the aperture array. Because of the inherent symmetric boundary conditions, such models simulate a single ion beamlet for an aperture located near the center of the optics grid. Hence, simulations using either axisymmetric codes or 3-D codes with hexagonal symmetric boundary conditions shall be referred to as *local beamlet* simulations in this paper. Existing modeling predictions of important ion optics parameters, such as the crossover limit, perveance limit, and backstreaming limit, are all based on extrapolations of local beamlet simulations, in which one uses different upstream plasma conditions to represent apertures at different locations on the grid surface. Previously, local beamlet simulations were carried out to model the impingement limit for the carbon-based ion optics (CBIO) gridlet [10,17]. Although the simulation gave good predictions of the perveance and backstreaming limits, it did not resolve the crossover limits for much of the operating voltage range. General disagreement between simulation and experimental crossover limits and the results from ongoing experimental studies at Colorado State University (CSU) suggests that the effects of geometric asymmetry from lack of adjacent holes and plasma sheath interaction between adjacent holes may have a significant influence on the crossover limit. Regardless of

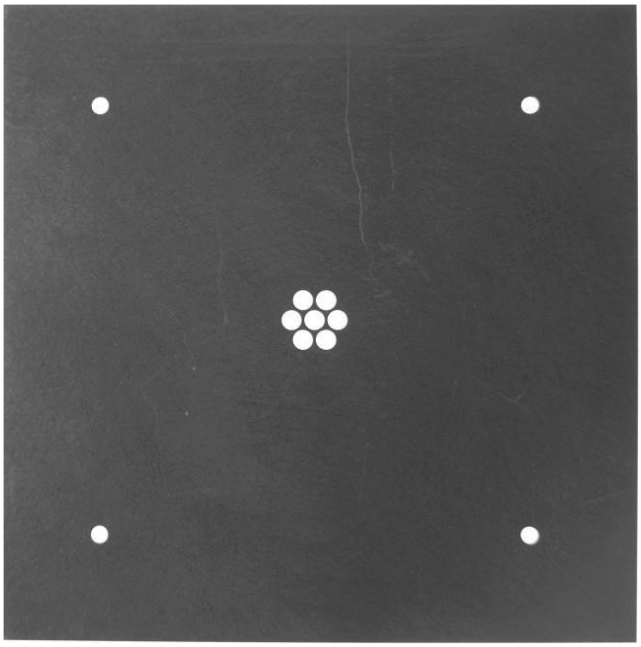

Fig. 1 Subscale CBIO-style Poco-graphite screen grid.

the reason, the current local beamlet models used by the electric propulsion community typically predicts a crossover limit value that can be 50 to 100% lower than the experimentally measured value.

A new ion optics model was developed recently by Kafafy and Wang [18] for three-dimensional simulations of plasma flow in an entire subscale ion optics system. This model explicitly includes apertures that are located both in the center and at the edge of the grid surface and fully accounts for the effects of multiple ion beamlets and geometric asymmetry. This new model was applied to simulate plasma flow in a seven-aperture optics gridlet and the results were compared with those from local beamlet simulations. It was shown that although a local beamlet model is adequate for modeling an aperture located in the center of the optics grid, it cannot resolve the quantitative differences in plasma sheath and beamlet behavior between an aperture that is completely surrounded by other apertures and circumferentially located apertures [18]. The ion optics model of [18], hereafter referred to as the *global gridlet model*, will be applied to study the crossover impingement in this paper.

This paper presents a coordinated experimental and numerical investigation of the crossover impingement for high-specific-impulse ion optics. The target of both the numerical and experimental studies is a seven-aperture ion optics gridlet. Although the experiments focus on accelerator-grid impingement-current measurement, the simulations also provide detailed information on ion optics plasma flow and the distribution of ion impingement on grid surfaces. The objective of this study is twofold. First, we would like to determine whether the global gridlet simulation model is able to correctly resolve the characteristics of direct beam-ion impingement and predict the crossover limit. Second, we would like to investigate whether experimental factors may have a noticeable effect on experimental predictions of the onset of crossover impingement.

Section II discusses the subscale ion optics gridlet used for this study and presents experimental results on accelerator-grid current.

Table 1 Dimensions of the subscale ion optics

Screen hole diameter d_s	2.305 mm
Screen-grid thickness t_s	0.461 mm
Acceleration hole diameter d_a	1.396 mm
Acceleration-grid thickness t_a	1.016 mm
Screen-to-acceleration-grid gap l_g	0.810 mm
Center-to-center hole spacing l_{cc}	2.674 mm

Section III discusses the simulation model and presents simulation results on plasma flow and direct ion impingement for both the center and edge apertures at crossover operating conditions. Section IV compares simulation results and measurements on accelerator-grid current characteristics and discusses factors affecting the prediction of the crossover limit. Section V contains a summary and conclusions.

II. Experimental Study

A. Subscale Gridlet

Subscale ion optics (gridlets) are often used to investigate the behavior of full-sized optics. The gridlets investigated here have a geometry identical to the screen and accelerator grids developed for the CBIO system [19]. The gridlets were fabricated at CSU from Poco graphite and were spaced from one another using standoff insulators. The apertures in the screen and accelerator gridlets were aligned through the use of holes placed at the four edges of each gridlet. Figure 1 shows the screen grid of the seven-aperture gridlet used for this study. Table 1 shows the geometrical parameters for the gridlets, and Table 2 lists some of the operating conditions considered in this study.

B. Experimental Results

The experimental investigation was carried out in a vacuum chamber with a volume of 0.65 m^3 and a base pressure in the midrange of 10^{-7} torr. When the ion source is running at typical xenon flow rates, the pressure is 1×10^{-5} torr. The vacuum chamber is equipped with a cryopump to eliminate the concern that an oil-based system would interfere with the experiments. The gridlets are placed 70 cm from a graphite target.

Tests were conducted by mounting an assembly composed of the two gridlet electrodes to a discharge chamber. The inner diameter of the discharge chamber is much larger than the active diameter of the gridlets to ensure that the discharge-chamber plasma properties are uniform over the entire gridlet area and to thereby impose common behavior in all beamlets. The uniform discharge plasma condition allowed division of the measured gridlet beam current J_B by the number of apertures to obtain the per-hole or per-beamlet current J_b. A ground screen is placed between most of the inactive area of the accelerator grid and the beam plasma to limit the collection of beam plasma ions on the inactive regions of the accelerator-gridlet surface. The impingement current collected by the entire accelerator grid J_A was converted to a per-beamlet value J_a by dividing by the number of active accelerator-grid apertures.

Figure 2 shows a typical measurement of the accelerator-grid impingement current for the seven-aperture gridlet (net accelerating voltage $V_N = 1600$ V). In the experiment, the beamlet current is varied by changing the discharge current while holding the discharge, beam, and accelerator voltages constant. The measured accelerator-grid impingement current J_a includes not only the

Table 2 Throttling conditions of the subscale ion optics

Net acceleration V_N, V	Screen-grid voltage V_s, V	Accelerator-grid voltage V_a, V	Total accelerating voltage V_T, V
800	770	−140	940
1000	970	−150	1150
1200	1170	−166	1366
1420	1390	−170	1590
1600	1570	−176	1776

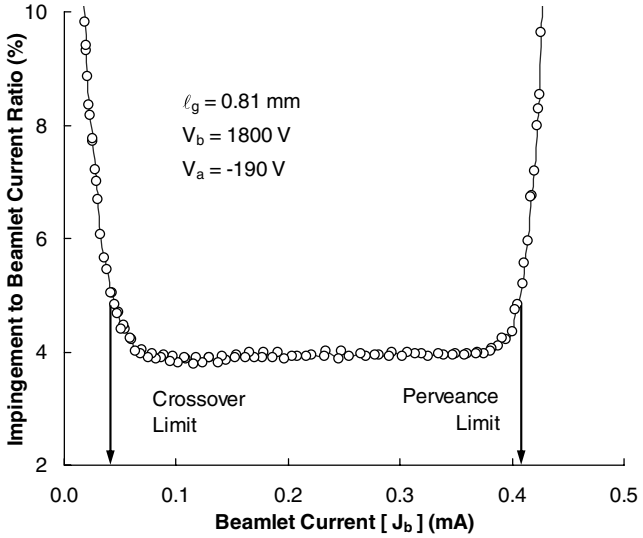

Fig. 2 Typical impingement limit data from experiment. Arrows indicate beamlet current in which direct impingement onset is defined as being 1% above baseline.

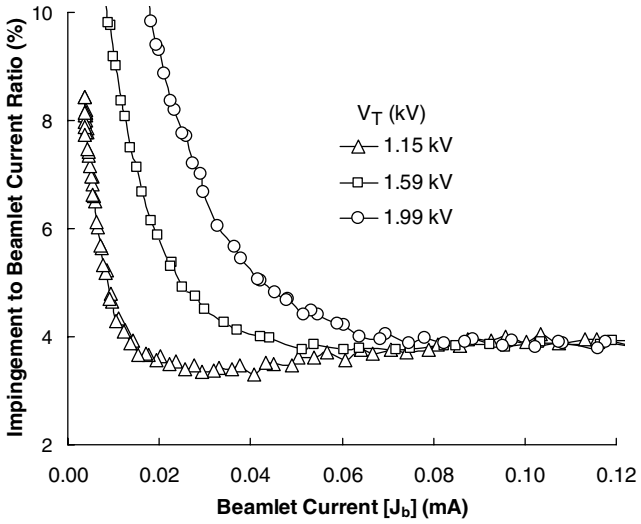

Fig. 3 Crossover impingement limit data from experiment showing effect of total voltage.

contribution from direct ion impingement J_{imp}, but also that from the collection of the charge-exchange ions J_{cex} and the leakage current in the system J_{leak}:

$$J_a = J_{\text{imp}} + J_{\text{cex}} + J_{\text{leak}} \tag{1}$$

The accelerator-grid impingement current displays a U shape when plotted as a ratio of impingement-to-beamlet current J_a/J_b, referred to herein as the relative impingement current typically measured in percent versus beamlet current. The left and right turning points on the U-shaped curve correspond to the crossover limit and perveance limit, respectively. At low beamlet currents, the relative impingement current rises due to crossover ion impingement on the downstream edge of the accelerator hole barrels. At moderate beamlet currents, the relative impingement current is flat and at a value dependent upon the background neutral density and the propellant utilization efficiency of the ion source. In our small vacuum facility operating at relatively low propellant utilization, the relative impingement current typically lies between 1 and 6% of the beam current. The neutral gas density and beamlet-current product is proportional to the amount of charge-exchange (CEX) production, resulting in steady CEX ion currents to the accelerator grid. As the beamlet current is increased to higher values, the relative impingement current will again rise quickly, indicating that direct ion interception is occurring on the upstream edge of the accelerator hole barrels due to perveance (or space-charge) limitations. Figure 3 further displays the relative accelerator-grid impingement current J_a/J_b for several selected total accelerating voltages at low beamlet currents. The measured accelerator current characteristics will be discussed further and compared with simulation predictions in Sec. V.

III. Simulation Study

A. Simulation Setup

The simulation study was carried out using the global gridlet simulation model described in [18]. This model is based on the hybrid-grid immersed-finite-element particle-in-cell (HG-IFE-PIC) algorithm [20], an extension of the immersed-finite-element particle-in-cell (IFE-PIC) algorithm [21,22]. The IFE-PIC algorithm is a hybrid immersed-finite-element finite difference particle-in-cell algorithm. A major feature of the IFE method is that it allows the use of a structured Cartesian mesh generated independently of the internal object boundary to solve problems involving complex internal boundaries while retaining the accuracy of unstructured body-fit mesh-based field solvers. In HG-IFE-PIC, we further allow the IFE and the PIC mesh nodes to be displaced from each other

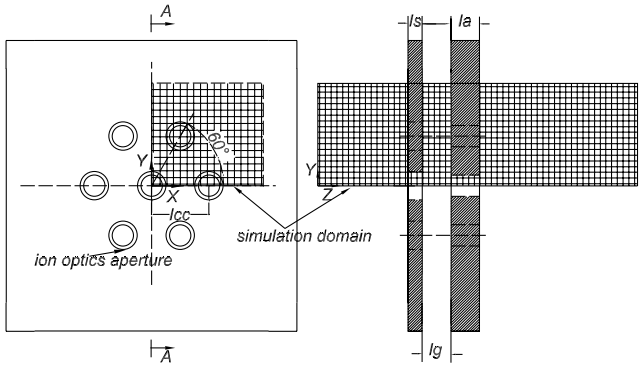

Fig. 4 Simulation setup.

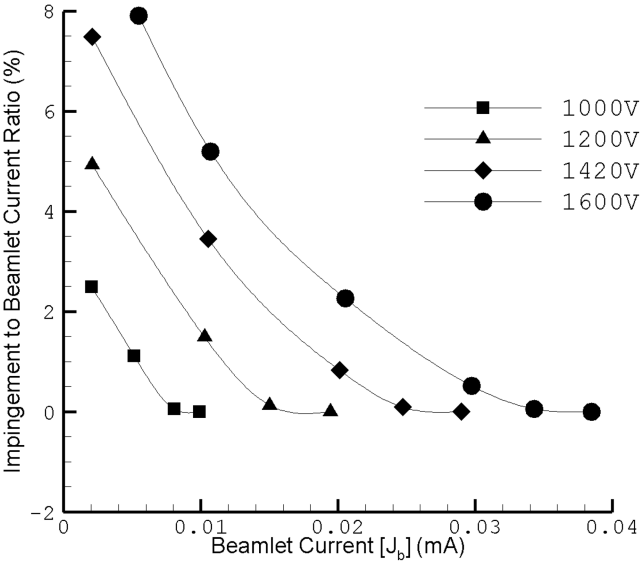

Fig. 5 Simulation results: direct impingement current for seven-hole gridlet at crossover.

instead of being collocated. We keep the uniform Cartesian mesh for PIC but stretch the primary IFE mesh according to the local potential and plasma gradients. This allows us to reduce the number of elements and mesh nodes used by IFE and to further increase the computational speed. In [18], a global gridlet model was developed using HG-IFE-PIC and a streamline approximation for beam-ion

flow. The global gridlet model explicitly includes apertures located near the edge of the grid surface and fully accounts for the effects of multiple ion beamlets and geometric asymmetry.

The simulation setup is shown in Fig. 4. The simulation domain is a three-dimensional rectangle domain that includes a quarter of the seven-aperture gridlet. This setup accounts for the geometric effects from a hexagonal layout of surrounded and circumferential apertures. In the beam flow direction, the upstream domain boundary is immersed in the discharge-chamber plasma. The ion extraction and the plasma sheath upstream of the accelerator grid are determined self-consistently. The downstream domain boundary is placed in the neutralized beam plasma. Symmetric boundary conditions are applied to the boundary surfaces at $x_{\min}$ and $y_{\min}$, and open boundary conditions are applied to the boundary surfaces at $x_{\max}$ and $y_{\max}$.

Macroparticles representing the propellant beam-ion streamlines are introduced into the simulation domain from the upstream boundary at each PIC time step. Each streamline is determined from the integration of its equation of motion given by Newton's second law as

$$\frac{\mathrm{d}}{\mathrm{d}t}(m\mathbf{v}) = \mathbf{F} = q\mathbf{E} \tag{2}$$

$$\mathbf{v} = \frac{\mathrm{d}\mathbf{x}}{\mathrm{d}t} \tag{3}$$

The electron density is considered to follow the Boltzmann distribution in the regions in which electrons exist (i.e., the upstream and downstream regions of the ion optics). Specifically, in the upstream region, the electron density is given by

$$n_e = n_{e0} \exp\left(\frac{e(\Phi - \Phi_0)}{kT_{e0}}\right) \tag{4}$$

where Φ_0, n_{e0}, and T_{e0} are the potential, electron density, and electron temperature of the discharge plasma, respectively. The downstream electron density is given by

$$n_e = n_{e\infty} \exp\left(\frac{e(\Phi - \Phi_\infty)}{kT_{e\infty}}\right) \tag{5}$$

where Φ_∞, $n_{e\infty}$, and $T_{e\infty}$ are the potential, electron density, and electron temperature of the downstream neutralized plasma, respectively. The electrostatic field is solved self-consistently with the boundary condition and the space charge of the particles from Poisson's equation:

$$\nabla \cdot (\epsilon_0 \nabla \Phi) = e(n_e - n_i) \tag{6}$$

Because the focus of this study is to simulate direct impingement by beam ions, simulations presented here only concern the flow of the propellant beam ions. Charge-exchange ions generated between the beam ions and neutrals are not included, to speed up the simulation. Charge-exchange ions have very little effect on the ion optics electric field and the beam-ion trajectories because of their negligible contribution to the overall space charge.

To calculate the beam-ion extraction properly, the upstream boundary needs to be set far from the screen grid and the cell size should resolve the Debye length of the upstream discharge plasma λ_{D0} [9]. Because the beam-ion density decreases rapidly in the downstream region of the acceleration grid, we allow the IFE mesh to stretch gradually in the downstream region. The stretched IFE mesh

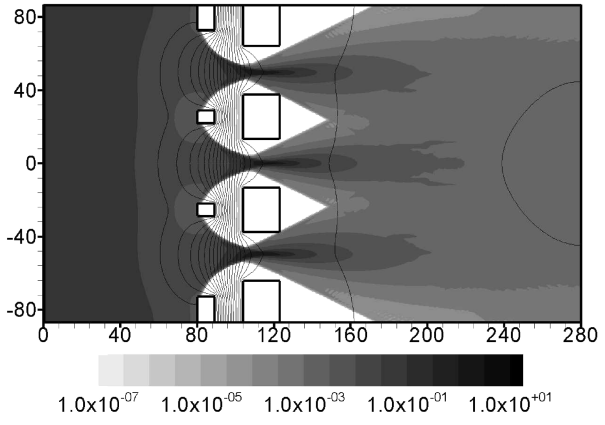

a) Y–Z plane

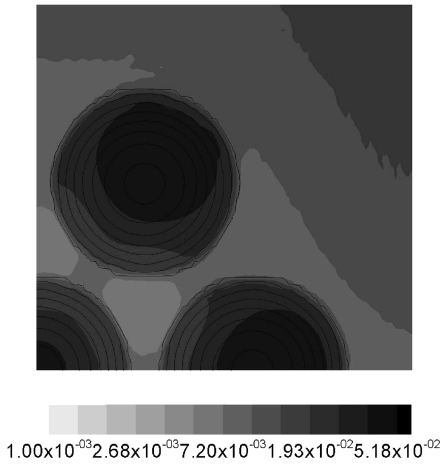

b) X–Y plane

Fig. 6 Simulation results: potential and beam-ion density contours; upstream plasma density is 1.5×10^{16} m^3.

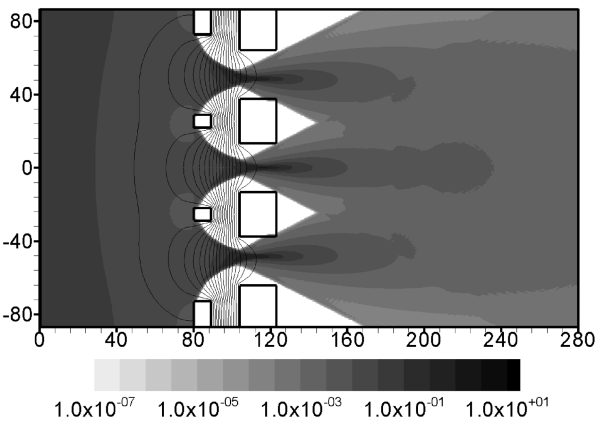

a) Y–Z plane

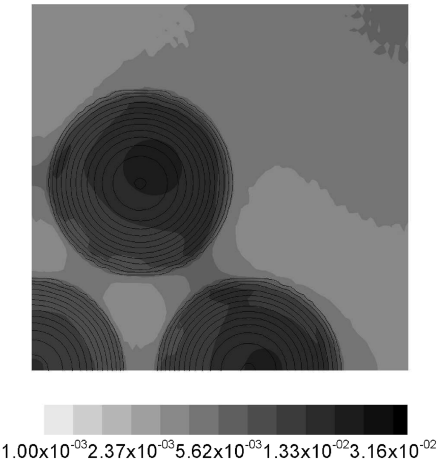

b) X–Y plane

Fig. 7 Simulation results: potential and beam-ion density contours; upstream plasma density is 0.5×10^{16} m^3.

is such that $\Delta z_{\min} \leq \lambda_{D0}$ and $\Delta z_{\max} < \lambda_{D\infty}$, where Δz is the length of the IFE base Cartesian cells in the z direction. In the lateral directions, we use a uniform mesh size. A typical simulation for results presented in this paper uses a uniform PIC mesh with $90 \times 52 \times 281$ cells and a stretched IFE mesh with more than 4.7 million finite elements, and it traces about 117,000 streamlines in each simulation step.

B. Simulation Results

This section presents simulation results on plasma flow through the subscale optics, accelerator-grid impingement current, and the distribution of ion impingement on grid surfaces. Simulations were carried out for all the operating conditions listed in Table 2. For each operating condition, we perform PIC simulations for a range of upstream plasma densities to scan for the impingement-current limit. Figure 5 shows simulation results on the relative accelerator-grid impingement current for several net accelerating voltages at low beamlet currents. The crossover onset for each operating condition is easily identified from these curves. These results will be discussed further in Sec. V.

Figures 6 and 7 show the potential and beamlet ion density contours for two upstream plasma conditions for a net accelerating voltage of $V_N = 1600$ V. In Fig. 6, the upstream density was set to be $n_0 = 0.15 \times 10^{17}$ m^{-3}. The beamlet current for this condition is about $J_b \simeq 0.03$ mA/hole, which is at the crossover limit (see Fig. 4). In Fig. 7, the upstream density was set to be $n_0 = 0.05 \times 10^{17}$ m^{-3}. The beamlet current for this condition is about $J_b \simeq 0.011$ mA/hole, which is below the crossover limit. The plots shown are for the x–z plane cutting through the middle of the gridlet and for the x–y plane at the upstream surface of the screen grid. Figures 8 and 9 show the distribution of ion impingement on the inside wall of both the center aperture and the edge apertures for the two upstream plasma conditions considered in Figs. 6 and 7, respectively.

In our previous simulations, we showed that the beamlet profile through the edge apertures is similar to the beamlet through the center aperture for normal operating conditions at beamlet currents greater than the crossover limit or at conditions near the perveance limit [18]. However, for operating conditions near the crossover limit, the beamlet through the edge aperture is asymmetrically focused more toward the optics center due to asymmetrically formed sheaths in the discharge plasma. The results shown in Figs. 6–9 further confirm this asymmetric feature. We find that for a multiple-aperture gridlet, direct beam-ion impingement of the accelerator grid at crossover onset is due to beam-ion impingement on the side wall of the edge apertures. The center-aperture barrel receives no direct impingement at the crossover onset. At operating conditions beyond the crossover limit, the impingement continues to concentrate on the inboard portion of the side wall of the edge apertures.

The asymmetric beamlet profile and impingement pattern are due to the sheath structure upstream of the screen grid. The sheath covering the edge aperture has a more convex curvature on the outboard portion of the aperture than the sheath covering the center aperture. Hence, the ions originated from outside the circumference of the sheath are more easily focused in the crossover direction, and the crossover limit for the edge aperture is different from that of the center aperture. As a result, direct impingement first occurs to the edge holes on the portion of the side wall oriented toward the inboard side when the operating condition is near crossover. Therefore, sputtering erosion would first occur to the edge apertures of the accelerator grid, and the erosion pattern on the edge apertures would

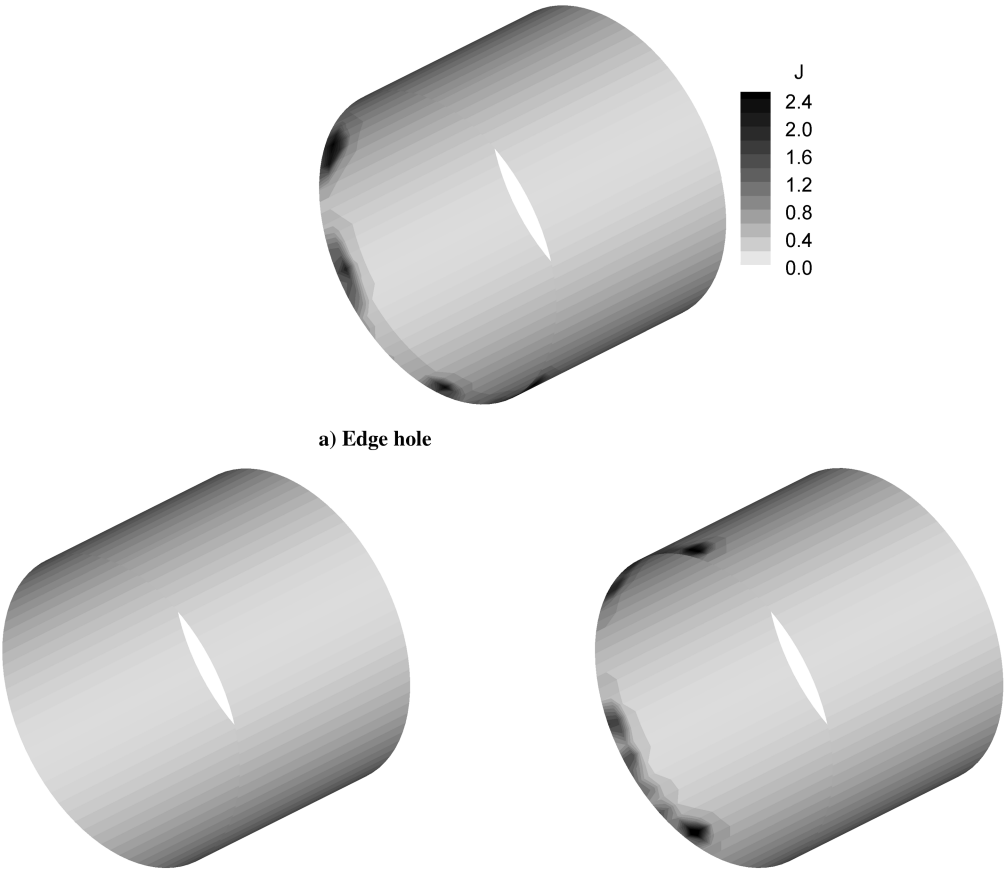

Fig. 8 Beam-ion impingement-current density distribution on the accelerator-grid center-aperture and edge-aperture side-wall surface; upstream plasma density is 1.5×10^{16} m^3; direct impingement onset starts at the inboard region of the edge-aperture barrel, whereas there is no direct impingement at the center aperture.

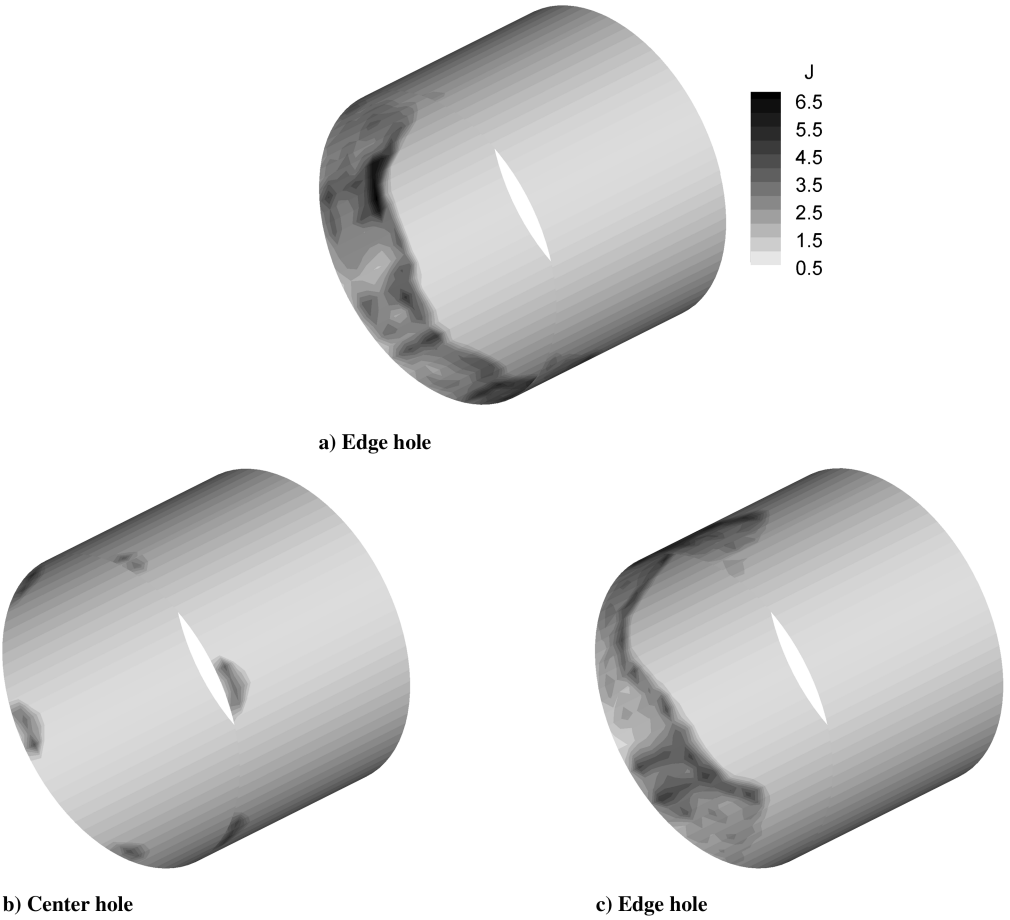

a) Edge hole

b) Center hole

c) Edge hole

Fig. 9 Beam-ion impingement-current density distribution on the accelerator-grid center-aperture and edge-aperture side-wall surface; upstream plasma density is 0.5×10^{16} m^3; there is already significant direct impingement at the inboard region of the edge-aperture barrel when impingement onset is starting at the center aperture.

be very asymmetrical. This asymmetric erosion pattern was also observed recently in the wear test of NASA's evolutionary xenon thruster (NEXT).

IV. Comparison of Simulation and Measurement

This section compares the accelerator-grid impingement-current characteristics and the crossover limits predicted by simulations with those obtained from experiments. It is important to note that this comparison will be affected by experimental factors that are not included in the simulation model and uncertainties in measurement. For instance, there will always be a systematic offset between the simulation obtained and measured impingement currents. Because the simulation model only includes the beam ions, the accelerator-grid current obtained from simulation includes only the contribution from beam-ion impingement (i.e., $J_a|_{\text{num}} = J_{\text{imp}}$). Hence, the relative accelerator impingement current from simulation can be expressed as

$$\left.\frac{J_a}{J_b}\right|_{\text{num}} = \frac{J_{\text{imp}}}{J_b} \tag{7}$$

On the other hand, the measured accelerator-grid current from experiments also includes the contributions from the CEX ions J_{cex} and the system leakage current J_{leak}. The contribution from J_{cex} may be easily identified in the measured data of J_a because the CEX current is proportional to the beam current:$J_{\text{cex}} \simeq CJ_b$. Hence, from Eq. (1), the measured relative accelerator-grid impingement current can be expressed as

$$\left.\frac{J_a}{J_b}\right|_{\text{exp}} = \frac{J_{\text{imp}}}{J_b} + C + \frac{J_{\text{leak}}}{J_b} \tag{8}$$

where C is approximately a constant, independent of either J_b or the accelerating voltage. The contributions from J_{leak} cannot be easily isolated, however, because we do not have the data required to determine the exact functional form of J_{leak} on J_b and V_T. In particular, no measurable leakage current exists when measurements are made with no ion extraction at the electric fields investigated in this study. Hence, J_{leak} is a major factor in measurement uncertainty. Another experimental factor that could introduce measurement uncertainty is the effect of discharge plasma property fluctuation on the measured accelerator current. All plasma sources have some finite level of plasma density fluctuation, which can be about 20% or more of the average plasma density. As a result, the experimental beamlet current will be fluctuating as well. This would cause rounding of the region near the onset of crossover. Nevertheless, because the crossover impingement is driven by direct impingement of the beam ions, one expects that the characteristics of the measured accelerator current curves $J_a/J_b|_{\text{exp}}$ will be dominated by those of J_{imp} once crossover occurs.

In Fig. 10, the experimental and numerical accelerator-grid impingement currents are plotted together for several accelerating voltages. From Eqs. (7) and (8), the offset between the $J_a/J_b|_{\text{num}}$ and $J_a/J_b|_{\text{exp}}$ curves reflects the effects from J_{cex} and experimental uncertainties such as J_{leak}. The offset in the y coordinate between the $J_a/J_b|_{\text{num}}$ and $J_a/J_b|_{\text{exp}}$ curves is primarily due to the contribution of J_{cex}. It is not surprising to find that the offset in the y coordinate is about the same for all of the cases considered. This is because J_{cex} is proportional to the beam current. The comparisons suggest that the contribution from charge-exchange ions to the accelerator current measured in experiments is approximately $J_{\text{cex}} \simeq 0.045J_b$. The offset in the x coordinate could be due to experimental uncertainties such as J_{leak} and/or numerical model artifacts. We find that the x coordinate offset is different for different accelerating voltages,

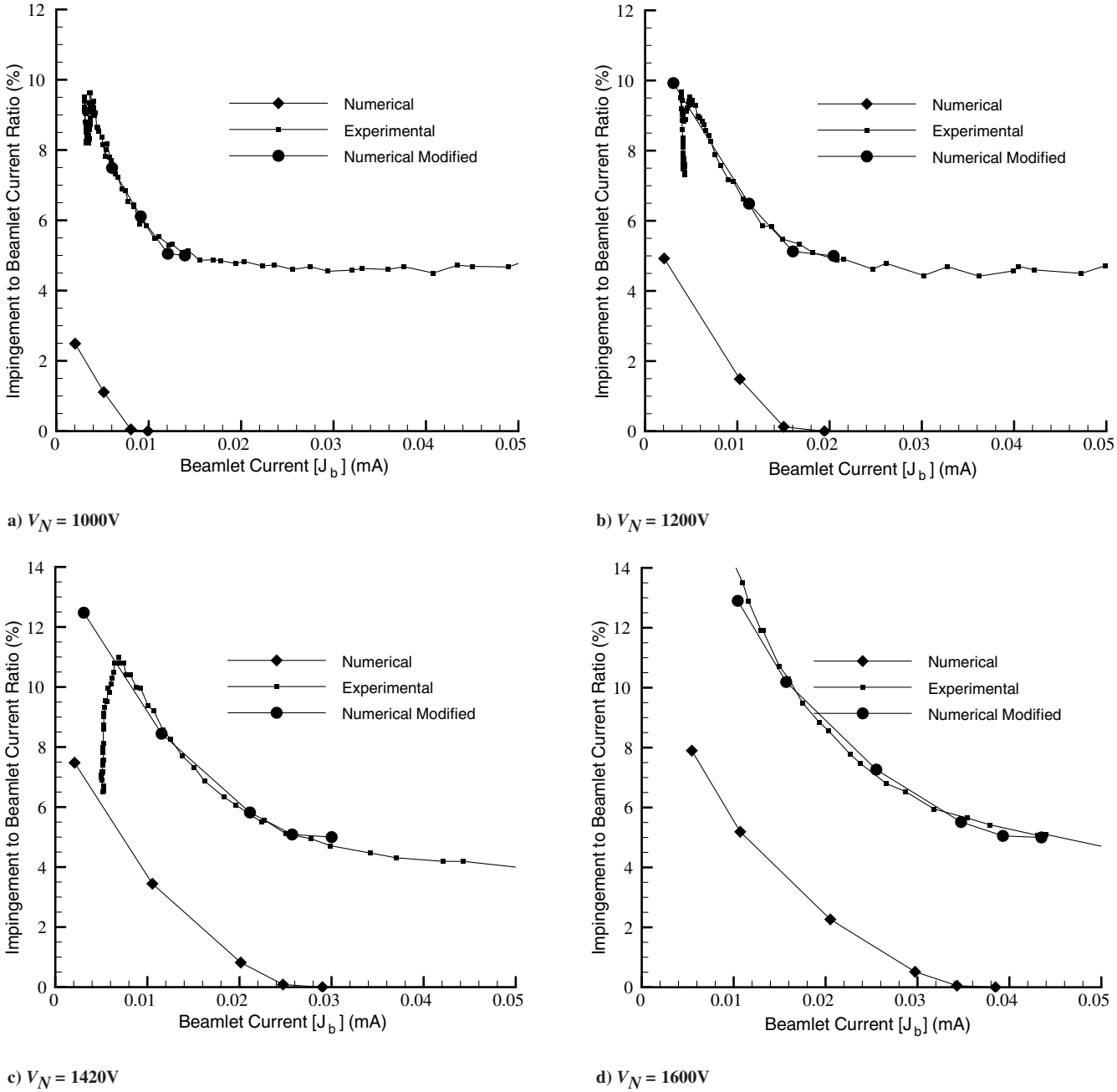

Fig. 10 Accelerator-grid impingement current: comparison of simulation and experimental results.

ranging from $\Delta J_b \simeq 0.001$ to 0.005 mA/hole. Although the exact locations of the $J_a/J_b|_{\text{exp}}$ curves are affected by J_{cex}, J_{leak}, and other experimental factors, the shape of these curves is determined primarily by the characteristics of direct beam-ion impingement J_{imp}, because J_{imp} dominates the measured accelerator-grid current once crossover impingement occurs. To compare the shape of the $J_a/J_b|_{\text{num}}$ curves, we further shift the $J_a/J_b|_{\text{num}}$ curves to overlap with the $J_a/J_b|_{\text{exp}}$ curves (labeled as "numerical modified" in Fig. 10). Note that the shifted curves are *not* used for predicting the crossover onset. We find that the shape of $J_a/J_b|_{\text{num}}$ matches that of $J_a/J_b|_{\text{exp}}$ almost perfectly in every case. Hence, we believe that the simulation model correctly predicts the behavior of direct ion impingement J_{imp} in experiments.

We next compare the experimental and simulation prediction of the crossover limit. The theoretical definition of the crossover limit is the value of J_b when direct beam-ion impingement current becomes nonzero:

$$J_{\text{imp}} \geq 0 \tag{9}$$

Although the theoretical definition is used in simulation, it is difficult to adopt the same definition in experiments, due to the difficulty in detecting onset in a precise and repeatable manner. As discussed previously, the measured accelerator-grid current includes not only beam-ion impingement, but also contributions from charge-exchange ions and system leakage current, and is affected by measurement uncertainties. Because of the contributions from J_{cex} and J_{leak}, plasma fluctuation effects on beam current, and the noise in accelerator and beam current measurements, the exact beamlet-current value at which J_{imp} first becomes larger than zero is not feasible to determine from the measurement. Hence, in experiments, we shall define the crossover limit as when $J_a/J_b|_{\text{exp}}$ becomes larger by a finite amount above the relative baseline current J_{baseline}/J_b, where

$$\frac{J_{\text{baseline}}}{J_b} = \frac{J_{\text{cex}}}{J_b} + \frac{J_{\text{leak}}}{J_b} \tag{10}$$

Our experimental crossover limit is defined as when

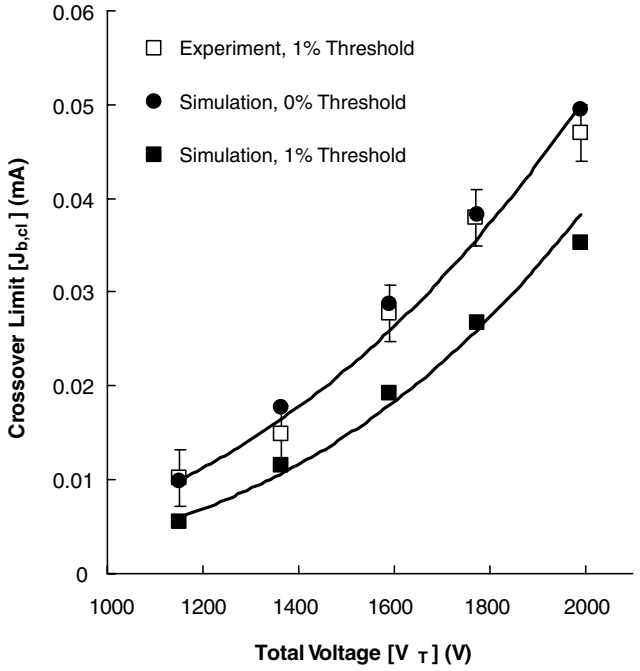

Fig. 11 Comparison of experimentally measured and numerically predicted crossover limits.

$$\left.\frac{J_a}{J_b}\right|_{\text{exp}} - \left.\frac{J_{\text{baseline}}}{J_b}\right|_{\text{exp}} = 0.01 \tag{11}$$

This will be referred to as the *experiment-1%-threshold* crossover limit. To perform a similar comparison, we shall also define a *simulation-1%-threshold* crossover limit from the $J_a/J_b|_{\text{num}}$ curves as

$$\left.\frac{J_a}{J_b}\right|_{\text{num}} = 0.01 \tag{12}$$

The value of $J_b|_{\text{num}}$ corresponding to the theoretical definition of the crossover limit [Eq. (9)] determined from the $J_a/J_b|_{\text{num}}$ curves will be referred to as the *simulation-0%-threshold* crossover limit.

Figure 11 compares the simulation-0%-threshold, simulation-1%-threshold, and experiment-1%-threshold crossover limits. Least-squares power-law fits of the simulation results are also plotted on the figures to show the dependence of the crossover limits on V_T. The measurements of J_b and J_a were made with a resolution equal to or better than 0.1%. Because the $J_a/J_b|_{\text{exp}}$ ratios are used to detect the beamlet current at the onset of crossover, we avoid the uncertainties induced by systematic error on J_a measurements. Hence, the error in the crossover beamlet-current determination is dominated by the average step resolution in J_b current that we used to collect data. In terms of a percent, the step resolution was about 4% of the crossover beamlet-current limit at $V_T = 2000$ V, which represents the worst-case estimate of the error on the measured crossover limit from known sources. Therefore, an error bar of $\pm 4\%$ is shown for the experimental results.

We find that the simulation-1%-threshold crossover limits fall within 20% of the experiment-1%-threshold crossover limits. This discrepancy reflects the x coordinate offset shown in Fig. 10 and is likely due to measurement uncertainties such as those from leakage current and plasma density fluctuations caused by plasma source and experimental aspects that are not included in the simulation model. These uncertainties will be addressed in a future study. It is interesting to note, however, that the simulation-0%-threshold results almost exactly match the experiment-1%-threshold results. More important, the scaling of the crossover limits obtained from experiment and that from simulation are very similar, all exhibiting a $V_T^{\sim 3}$ power-law dependence.

V. Conclusions

Experimental and modeling studies were carried out to investigate crossover ion impingement for a seven-aperture CBIO-like gridlet. Simulation predictions of the accelerator-grid impingement current and the crossover limits using a new three-dimensional global gridlet model agree well with the measurements. We find that the model almost exactly reproduces the characteristics of direct beam-ion impingement contained in the measured data when contributions from the charge-exchange ions and the leakage current in experiments are taken into account. The crossover limits from simulation also show the same power-law dependence on the total voltage as that from measurements. Comparisons between simulation and experiment also suggest that although the contribution from the charge-exchange ions can be easily identified in the data, the contributions from the leakage current and other experimental factors cannot be easily isolated. Such uncertainties will have a noticeable effect on the prediction of the crossover onset and will need to be quantified further in subsequent studies. Simulations also show that at near-crossover operating conditions, the beamlets through edge apertures are asymmetrically focused more toward the optics center, due to focusing of the ions originating from outside the circumference of the sheath covering the edge apertures. As a result, direct impingement first occurs on edge holes on the portion of the hole barrel oriented toward the center when the operating condition is near crossover. Hence, the crossover onset for the edge apertures is different from center apertures or apertures surrounded by other apertures. Consequently, the accelerator grid would experience significantly more erosion on the edge holes, due to direct ion impingement at crossover. Predictions based on local beamlet simulations would either miss this important process entirely or significantly underpredict its severity.

References

[1] Peng, X., Keefer, D., and Ruyten, W., "Plasma Particle Simulation of Ion Thrusters," *Journal of Propulsion and Power*, Vol. 8, No. 2, 1992, pp. 361–366.

[2] Hayakawa, Y., "Three-Dimensional Numerical Model of Ion Optics System," *Journal of Propulsion and Power*, Vol. 8, No. 1, 1992, pp. 110–117.

[3] Arakawa, Y., and Nakano, M., "An Efficient Three-Dimensional Optics Code for Ion Thruster Research," 32nd AIAA/ASME/SAE/ASEE Joint Propulsion Conference and Exhibit, Lake Buena Vista, FL, AIAA Paper 96-3198, July 1996.

[4] Tartz, M., Hartmann, E., Deltaschew, R., and Neumann, H., "Grid Erosion Study of a Three-Dimensional Ion Thruster," 34th AIAA/ASME/SAE/ASEE Joint Propulsion Conference and Exhibit, Cleveland, OH, AIAA Paper 98-3646, July 1998.

[5] Muravlev, V. A., and Shagayda, A. A., "Numerical Modelling of Extraction Systems in Ion Thrusters," 26th International Electric Propulsion Conference, Kitakyushu, Japan, International Electric Propulsion Conference Paper 99-162, July 1999.

[6] Okawa, Y., and Takegahara, H., "Particle Simulation on Ion Beam Extraction Phenomena in an Ion Thruster," 26th International Electric Propulsion Conference, Kitakyushu, Japan, International Electric Propulsion Conference Paper 99-146, July 1999.

[7] Boyd, I. D., and Crofton, M. W., "A Computational Study of Grid Erosion Through Ion Impact," 36th AIAA/ASME/SAE/ASEE Joint Conference and Exhibit, Huntsville, Alabama, AIAA Paper 00-3664, July 2000.

[8] Nakayama, Y., and Wilbur, P. J., "Numerical Simulation of Ion Beam Optics for Multiple-Grid Systems," *Journal of Propulsion and Power*, Vol. 19, No. 4, 2003, pp. 607–613.

[9] Wang, J., Polk, J., Brophy, J., and Katz, I., "Three-Dimensional Particle Simulations of Ion Optics Plasma Flow and Grid Erosion," *Journal of Propulsion and Power*, Vol. 19, No. 6, 2003, pp. 1192–1199.

[10] Farnell, C. C., Williams, J. D., and Wilbur, P. J., "NEXT Ion Optics Simulation Via ffx," 39th AIAA/ASME/SAE/ASEE Joint Propulsion Conference and Exhibit, Huntsville, AL, AIAA Paper 03-4869, July 2003.

[11] Farnell, C., "Numerical Simulation of HiPEP Ion Optics," 40th AIAA/ASME/SAE/ASEE Joint Propulsion Conference and Exhibit, Fort Lauderdale, FL, AIAA Paper 04-3818, July 2004.

[12] Anderson, J., Katz, I., and Goebel, D., "Numerical Simulation of Two-Grid Ion Optics Using a 3D Code," 40th AIAA/ASME/SAE/ASEE

Joint Propulsion Conference and Exhibit, Fort Lauderdale, FL, AIAA Paper 04-3814, July 2004.

[13] Malone, S., and Soulas, G., "Computational Ion Optics Design Evaluations," 40th AIAA/ASME/SAE/ASEE Joint Propulsion Conference and Exhibit, Fort Lauderdale, FL, AIAA Paper 04-4869, July 2004.

[14] Emhoff, J. W., and Boyd, I. D., "Grid Erosion Modeling of the NEXT Ion Thruster Optics," 39th AIAA/ASME/SAE/ASEE Joint Propulsion Conference and Exhibit, Huntsville, AL, AIAA Paper 03-4868, July 2003.

[15] Emhoff, J. W., and Boyd, I. D., "Progress In NEXT Ion Optics Modeling," 40th AIAA/ASME/SAE/ASEE Joint Propulsion Conference and Exhibit, Fort Lauderdale, FL, AIAA Paper 04-3786, July 2004.

[16] Emhoff, J. W., and Boyd, I. D., "NEXT Ion Optics Modeling of Total Thruster Performance," 41st AIAA/ASME/SAE/ASEE Joint Propulsion Conference and Exhibit, Tucson, AZ, AIAA Paper 05-3687, July 2005.

[17] Laufer, D. M., Williams, J. D., Farnell, C. C., Shoemaker, P. B., and Wilbur, P. J., "Experimental Evaluation of Sub Scale CBIO Ion Optics Systems," 39th AIAA/ASME/SAE/ASEE Joint Propulsion Conference and Exhibit, Huntsville, AL, AIAA Paper 03-5165, July 2003.

[18] Kafafy, R., and Wang, J., "Whole Ion Optics Gridlet Simulations Using a Hybrid-Grid IFE-PIC Code," *Journal of Propulsion and Power*, Vol. 23, No. 1, 2007, pp. 59–68.
doi:10.2514/1.21346

[19] Snyder, J., and Brophy, J., "Performance Characterization and Vibration Testing of 30-cm CarbonCarbon Ion Optics," 40th AIAA/ASME/SAE/ASEE Joint Propulsion Conference and Exhibit, Ft. Lauderdale, FL, AIAA Paper 2004-3959, July 2004.

[20] Kafafy, R., and Wang, J., "A Hybrid-Grid Immersed-Finite-Element Particle-in-Cell Algorithm for Modeling Spacecraft Plasma Interactions," *IEEE Transactions on Plasma Science*, Vol. 34, No. 5, 2006, pp. 2114–2124.
doi:10.1109/TPS.2006.883404

[21] Wang, J., Cao, Y., Kafafy, R., Pierru, J., and Decyk, V., "Ion Propulsion Plume Simulations Using Parallel Supercomputer," *IEEE Transactions on Plasma Science*, Vol. 34, No. 5, 2006, pp. 2148–2158.
doi:10.1109/TPS.2006.883406

[22] Kafafy, R., Lin, T., Lin, Y., and Wang, J., "Three Dimensional Immersed Finite Element Methods for Electric Field Simulation in Composite Materials," *International Journal for Numerical Methods in Engineering*, Vol. 64, Aug. 2005, pp. 940–972.
doi:10.1002/nme.1401

A. Gallimore
Associate Editor